Chemically-Linked Heterostructures of Palladium Nanosheets and 2H-MoS$_2$

Ramiro Quirós-Ovies, Pablo Bastante, Simon Hettler, Víctor Vega-Mayoral, Sergio Aina, Vasileios Balos, Thomas Pucher, Andrés Castellanos-Gomez, Raul Arenal, Juan Cabanillas-Gonzalez, Emilio M. Pérez,* Jesús Santamaría, and Víctor Sebastian*

The burgeoning field of 2D heterostructures targets the combination of 2D materials with 3D, 1D, or 0D nanomaterials. Among the most popular 2D materials, the 2H polytype of molybdenum disulfide (MoS$_2$) features a well-defined bandgap that becomes direct at the monolayer level, which can be exploited for photodetection. A notable limitation of 2H-MoS$_2$ is its curtailed absorbance beyond the visible range. Here, a covalently-linked Pd nanosheet (PdNS)/functionalized MoS$_2$ (*f*-MoS$_2$) heterostructure is introduced, leveraging PdNS infrared-absorbing properties to surmount this constraint. A bifunctional molecule, featuring a maleimide for attachment to MoS$_2$ and a phenyl bromide for connection to PdNS, enables the synthesis of the heterostructure. Comprehensive spectroscopic and microscopic characterization shed light on the structure of PdNS@*f*-MoS$_2$ and the electronic interaction between its components. Prototype devices show an enhancement in the width and intensity of the optoelectronic response of PdNS@*f*-MoS$_2$ in the infrared, up to 1700 nm. In comparison, a van der Waals heterostructure with the same components shows poorer photoresponse. The results prove that the covalent linkage of metal nanostructures to 2D materials is a promising approach to build mixed-dimensional heterostructures.

1. Introduction

The past decade has witnessed a significant increase in the study of mixed-dimensional heterostructures,[1–4] which involve the integration of 0D, 1D, 2D, and 3D nanomaterials.[5] The intrinsic properties of the nanomaterials, combined with the current tools to connect these structures by several approaches,[6–10] appears to be the new playground for material science researchers, as the resulting structures show a vast amalgam of optoelectronic,[11–22] energy storage,[23–26] and catalytic[27–29] applications. The general hypothesis behind these research efforts is that the properties of the individual components forming the heterostructure will combine synergistically or, at least without any detrimental effects upon the formation of the heterostructure. A key question in this sense is the interface between the nanomaterials. The vast majority of heterostructures reported so far

R. Quirós-Ovies, S. Hettler, S. Aina, R. Arenal, J. Santamaría, V. Sebastian
Instituto de Nanociencia y Materiales de Aragón (INMA)
CSIC-Universidad de Zaragoza
Zaragoza 50009, Spain
E-mail: victorse@unizar.es
R. Quirós-Ovies, V. Vega-Mayoral, V. Balos, J. Cabanillas-Gonzalez, E. M. Pérez
IMDEA Nanociencia
Ciudad Universitaria de Cantoblanco
Madrid 28049, Spain
E-mail: emilio.perez@imdea.org

P. Bastante
Departamento de Física de la Materia Condensada
Universidad Autónoma de Madrid
Madrid 28049, Spain
S. Hettler, R. Arenal, V. Sebastian
Laboratorio de Microscopías Avanzadas
Universidad de Zaragoza
Zaragoza 50018, Spain
T. Pucher, A. Castellanos-Gomez
2D Foundry Group
Instituto de Ciencia de Materiales de Madrid (ICMM-CSIC)
Madrid 28049, Spain
R. Arenal
ARAID Foundation
Zaragoza 50018, Spain
J. Santamaría, V. Sebastian
Networking Research Center on Bioengineering
Biomaterials and Nanomedicine (CIBER-BBN)
Madrid 28029, Spain

**ADVANCED
SCIENCE NEWS**
www.advancedsciencenews.com

NANO · MICRO
small
www.small-journal.com

are based on direct contact of the nanomaterials through van der Waals forces, to the point that they are known as van der Waals heterostructures.[30] Among the few reported covalently linked heterostructures, the conjugation of MoS_2 with carbon nanohorns enhanced electrocatalytic activity for proton reduction.[31] We recently introduced an alternative method for creating 2D–2D heterostructures through the covalent linkage of graphene and MoS_2.[32]

In the present work, we synthesize and characterize a chemically linked mixed-dimensional heterostructure composed of Pd nanosheets (PdNS) and 2H-MoS_2 and explore its potential application in broad-band photodetectors. We use PdNS to provide absorption in the near infrared (NIR) and 2H-MoS_2 for ultraviolet–visible (UV–vis) absorption and photodetection, and we connect both materials covalently through a bifunctional molecule featuring chemically orthogonal groups: a maleimide for connection to MoS_2,[33] and bromophenyl to link to PdNS.

There are only a few previous examples of van der Waals Pd/MoS_2 heterostructures, synthesized employing chemical vapor deposition (CVD)[34–38] or solution-based methods.[39] For example, Tian-Ling Ren et al.[40] integrated a MoS_2/Pd nanoparticles (NPs) interface in a resistive random-access memory (RRAM) structure based on ITO/HfO_2/MoS_2/Pd to optimize its performance in comparison with a MoS_2 device. The RRAM demonstrated large stability and data retention properties, with no obvious degradation even at higher temperatures. Meanwhile, Pandey[41] where a Pd-modified reduced graphene oxide (RGO)-supported MoS_2 heterostructure (RGO/MoS_2/Pd) was synthesized for water splitting electrocatalysis. To the best of our knowledge, the covalent linkage of Pd nanomaterials and 2H-MoS_2 is completely unexplored

The MoS_2 flakes were exfoliated using a novel exfoliation procedure reported by our group and based on an ultrafast heating of MoS_2 intercalated solvent by microwave irradiation.[42] For the on-device characterization, mechanically exfoliated MoS_2 was employed. Both methods ensure the production of ultrathin, yet large-area flakes, suitable for subsequent Pd film incorporation. PdNS, synthesized by a high-pressure CO reduction of Pd precursor (Na_2PdCl_4), are Pd based nanostructures with a surface plasmon resonance (SPR) in the NIR.[43] The ultrathin structure (≈ 1.5 nm) endows this material with an outstanding absorbance in the infrared region (from 800 to 1600 nm) with a main peak at 1000 nm. PdNS were eventually connected to the MoS_2 flakes assisted by the *N*-(4-bromophenyl)maleimide (MalPhBr) functionalization, as illustrated in **Scheme 1**.

2. Results and Discussion

### 2.1. Synthesis of Pd Nanosheets, MoS_2 Functionalization, and Heterostructure Assembly

As mentioned above, MoS_2 flakes were exfoliated using a procedure previously reported by our group, based on ultrafast heating

by microwave irradiation,[42] which ensures the production of ultrathin yet large-area flakes, suitable for subsequent PdNS incorporation. Following this, the maleimide was grafted onto MoS_2 as it is detailed in our previous work.[33,44] The appropriate selection of the maleimide molecule was critical for the successful bonding between the two materials. A systematic testing of a library of different maleimides was performed to determine which functional group had the highest affinity for other Pd nanostructures, as depicted in Figure S1 in the Supporting Information. We found that MalPhBr exhibited the best performance, leading us to choose this molecule for the heterostructure connection. This finding aligns well with the established understanding that many coupling reactions utilize aryl bromide derivatives for the oxidative addition phase in the cross-coupling mechanism.[45] PdNS were synthesized by a 6 bar CO reduction of Pd precursor (Na_2PdCl_4) and eventually linked to the functionalized MoS_2 flakes (*f*-MoS_2). The attachment of PdNS onto the *f*-MoS_2 was achieved by mildly stirring the two components in acetonitrile (ACN) for 16 h, facilitated by the bromine-terminated maleimide functionalization, as illustrated in Scheme 1. Upon completion of the reaction, purification involved three centrifugation cycles at 10 000 rpm for 10 min, using ACN to remove unbound PdNS.

The formation of the covalent bond between the sulfur of the layered material and the succinimide was confirmed using Attenuated Total Reflectance-Fourier Transform Infrared (ATR-FTIR) spectroscopy (as depicted in **Figure 1b,c**). The characteristic peaks of the organic moiety (illustrated by the green line in Figure 1b) are evident in the *f*-MoS_2-MalPhBr spectrum (red line in Figure 1b). The disappearance of the strong alkene C−H bending mode, at 810 cm^{-1} in the spectrum of MalPhBr (green trace), and the visible specific C−S bond at 720 cm^{-1},[46,47] is shown in Figure 1c. Thermogravimetric Analysis (TGA) shown in Figure 1d reveals a weight discrepancy of $\approx 10\%$ between the exfoliated (black line) and functionalized (red line) MoS_2, attributable to the organic moiety.

Concerning the formation of thin PdNS,[43] CO acts as both reductant and as a capping agent in the formation of PdNS, due to its binding affinity on certain facets (Figure S2, Supporting Information).[48] This selective adsorption significantly affects the shape of the nanocrystal and promotes the anisotropic growth into ultrathin nanosheets of less than 9 atomic layers.[43] Transmission Electron Microscopy (TEM) images in Figure 1e–g depict the morphology of PdNS. Following particle size analysis resulted in a mean lateral size of 35 ± 7 nm. These dimensions lead to the broad SPR absorption shown in Figure 1a (orange line). The synthesis of PdNS can be achieved using various solvents, resulting in similar morphologies and dimensions (see Figures S3–S4, Supporting Information). Initially, PdNS were synthesized in *N*-methyl-2-pyrrolidone (NMP, Figure S3, Supporting Information) due to its utilization in the exfoliation of MoS_2, aiming to streamline the process by reducing the number of reagents. However, given the subsequent transfer of MoS_2 into ACN for maleimide functionalization and heterostructure synthesis, PdNS were also transferred to ACN. In this case, it was observed that NMP residue was more challenging to eliminate, resulting in a higher degree of contamination in the PdNS@MoS_2 heterostructure. Consequently, PdNS were synthesized using DMF and CO under high pressure

J. Santamaría, V. Sebastian
Department of Chemical and Environmental Engineering
Campus Rio Ebro
Universidad de Zaragoza
Zaragoza 50018, Spain
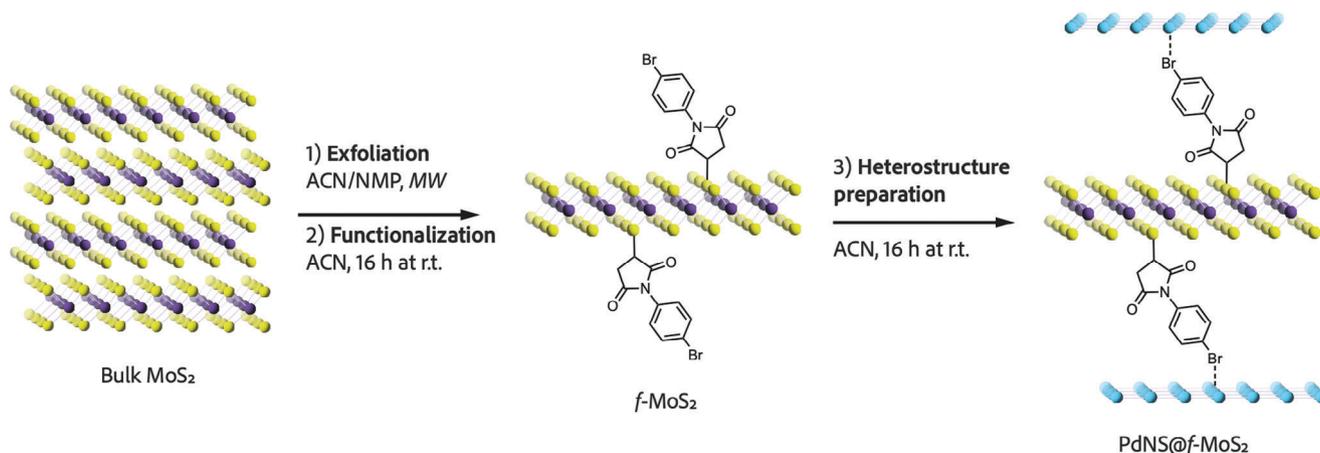
Scheme 1. Graphic representation illustrating the process of bulk MoS_2 exfoliation (**1**) and subsequent functionalization with MalPhBr (**2**), where sulfur (S) is depicted by yellow spheres and molybdenum (Mo) by purple spheres. This is followed by the attachment of PdNS (**3**), which are represented by light blue spheres, onto the surface of the 2D material for heterostructure synthesis. For clarity, exfoliated MoS_2 and PdNS are schematized as monolayers, although they are not expected to be monolayers in the actual structures.
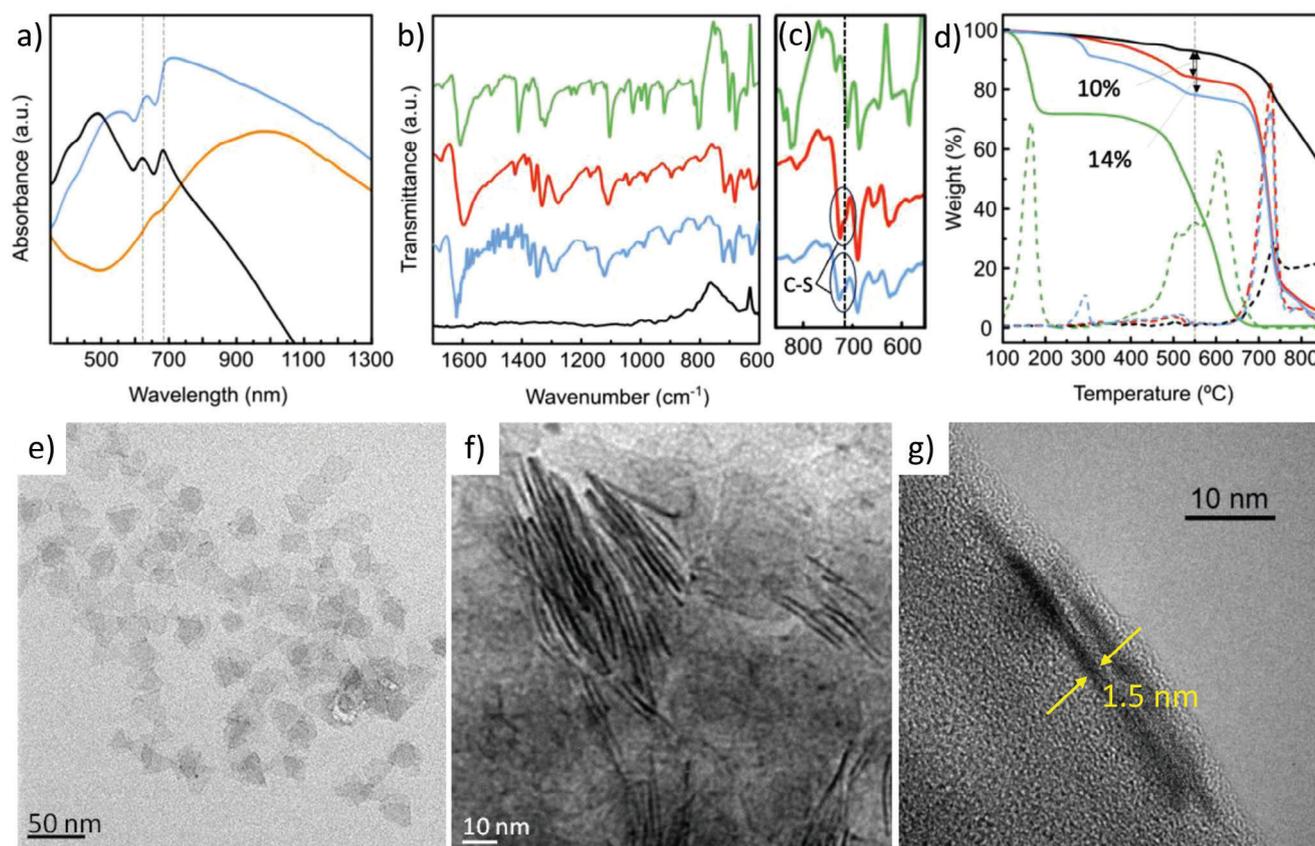

Figure 1. a) UV–vis–NIR spectroscopy of MW-exfoliated MoS_2 (black), PdNS (orange), and PdNS@f-MoS_2 heterostructure (blue). Dashed lines indicate the two main MoS_2 exciton signals, only noticeable when 2H-MoS_2 is appropriately exfoliated. b) ATR-FTIR spectra of the MW-exfoliated MoS_2 (black), MalPhBr (green), f-MoS_2-MalPhBr (red), and PdNS@f-MoS_2 heterostructure (blue). c) Zoomed ATR-FTIR spectra in the 550–850 cm^{-1} region, where the C—S bond (dashed line, 720 cm^{-1}) is observable, and d) Thermogravimetric Analysis (TGA) of the MW-exfoliated MoS_2 (black), PdNS (orange), MalPhBr (green), f-MoS_2-MalPhBr (red), and PdNS@f-MoS_2 heterostructure (blue). The dotted line at 550 °C indicates the temperature at which it is expected that all organic functionalization has been lost and material decomposition has not yet begun. e–g) TEM images of PdNS at different magnifications seen e) on-plane and f,g) in cross-section. Faced yellow arrows in (g) indicate the typical thickness of a PdNS.
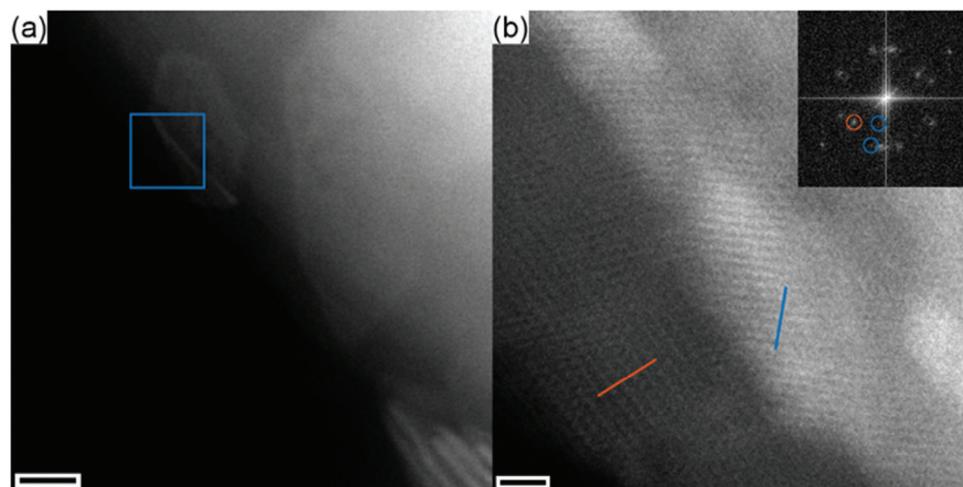
Figure 2. HAADF-STEM images of a MoS$_2$ flake with PdNS. a) Several PdNS are attached both vertically and horizontally to the flake. b) At high magnification, the MoS$_2$ lattice is clearly revealed with the [100] reflection marked by an orange line and a circle (inset fast Fourier transform (FFT)). The [200] Pd lattice planes are also observed (marked blue). Scale bars are a) 10 nm and b) 1 nm. Inset FFT width 16 nm^{-1}.

(6 bar, Figure S4, Supporting Information), transferred into ACN and then mixed with f-MoS$_2$-MalPhBr to form the final heterostructure.

UV–vis spectroscopic analysis highlighted the heterostructure's broad-spectrum absorbance, encompassing ultraviolet, visible, and infrared regions (blue line in Figure 1a), which shows basically a direct combination of the inherent absorbance of exfoliated MoS$_2$ within the UV–visible spectrum (represented by the black line in Figure 1a) and the corresponding absorbance of PdNS in the infrared range (depicted by the orange line). The PdNS@f-MoS$_2$-MalPhBr absorption spectra is, however, not a linear combination of the isolated PdNS and bare MoS$_2$ absorption spectra, indicating certain degree of hybridization between both kind of nanosheets (see transient absorption measurements below). The persistence of the C—S bond after attachment of the PdNS and further purification was confirmed by ATR-FTIR spectroscopy (represented by the blue line in Figure 1b,c). Furthermore, TGA indicated an augmented weight difference between the functionalized material and the resultant heterostructure, suggesting a Pd loading of ≈ 4 % relative to the f-MoS$_2$ (Figure 1d).

X-Ray Photoelectron Spectroscopy (XPS) analysis has been performed to PdNS@f-MoS$_2$-MalPhBr to identify the oxidation states of palladium and to confirm the functionalization of the exfoliated MoS$_2$ through the MalPhBr molecule. The Pd 3d detailed region shows one main component at 335.2 eV attributed to metallic Pd (0)$_{5/2}$, predominant in the PdNS (Figure S5a, Supporting Information). Subsequently, a second component is identified at 337.1 eV corresponding to Pd (II)$_{5/2}$.[49] Additionally, Pd (II) shifting to higher energy bindings is characteristic of its interaction with halides.[49,50] Furthermore, the interaction between PdNS and MalPhBr molecule is confirmed in the Br 3d detailed region (Figure S5c, Supporting Information). The component at lower energy bindings, 67.6 eV, is representative of the interaction between bromide and palladium, suggesting the successful bonding between the PdNS and the maleimide.[51] The higher energy binding component at 70.3 eV corresponds to the C—Br bond of the MalPhBr molecule.[51]

2.2. Structural Analysis of Functionalized PdNS@f-MoS$_2$ by Electron Microscopy and Spectroscopy

After confirming the successful synthesis of PdNS@f-MoS$_2$-MalPhBr, we delved deeper into the analysis of the heterostructure using TEM, Scanning (S)TEM and Electron Energy-Loss Spectroscopy (EELS) to obtain further information on the functionalization process of the hybrid PdNS and MoS$_2$ flakes. TEM and STEM images of the PdNS@f-MoS$_2$ heterostructure illustrate the orthogonal (Figures S6a and S7, Supporting Information) and parallel (Figures S6b and S7, Supporting Information) connection between both structures. **Figure 2a** shows a High-Angle Annular Dark Field (HAADF)-STEM image obtained from the edge of a MoS$_2$ flake on which several bright lines and larger brighter regions can be distinguished. These bright lines and regions correspond to PdNS, which are either vertically (lines) or horizontally (regions) oriented with respect to the image plane. When zooming in on one of the lines (Figure 2b), the image reveals both the MoS$_2$ lattice ([100] orientation is marked exemplarily by orange line and circle) as well as the [200] atomic planes of the PdNS (blue line and circles). As the analyzed region of the MoS$_2$ flake is suspended in vacuum, the PdNS are directly linked to the MoS$_2$.

To further investigate the material system, both STEM-EELS and STEM-Energy-Dispersive X-Ray spectroscopy (EDX) data have been obtained. **Figure 3a** shows a dark-field (DF)-STEM image of a MoS$_2$ flake. While the left edge is folded up, small brighter regions on a background with homogeneous dark intensity can be recognized in the central area of the flake. The comparison of the EDX signals obtained from the background and brighter regions (Figure 3c) reveals the presence of Mo and S in both, but only Pd in the latter (whole spectra in Figure S12, Supporting Information). Additional STEM-EDX analyses are shown in Figures S8–S11 in the Supporting Information. A closer look at the edge of such a brighter region allows the identification of several PdNS in both horizontal and vertical orientation attached to the MoS$_2$ flake (Figure 3b). Monochromated STEM-EELS has been performed in this edge region as marked in Figure 3b and
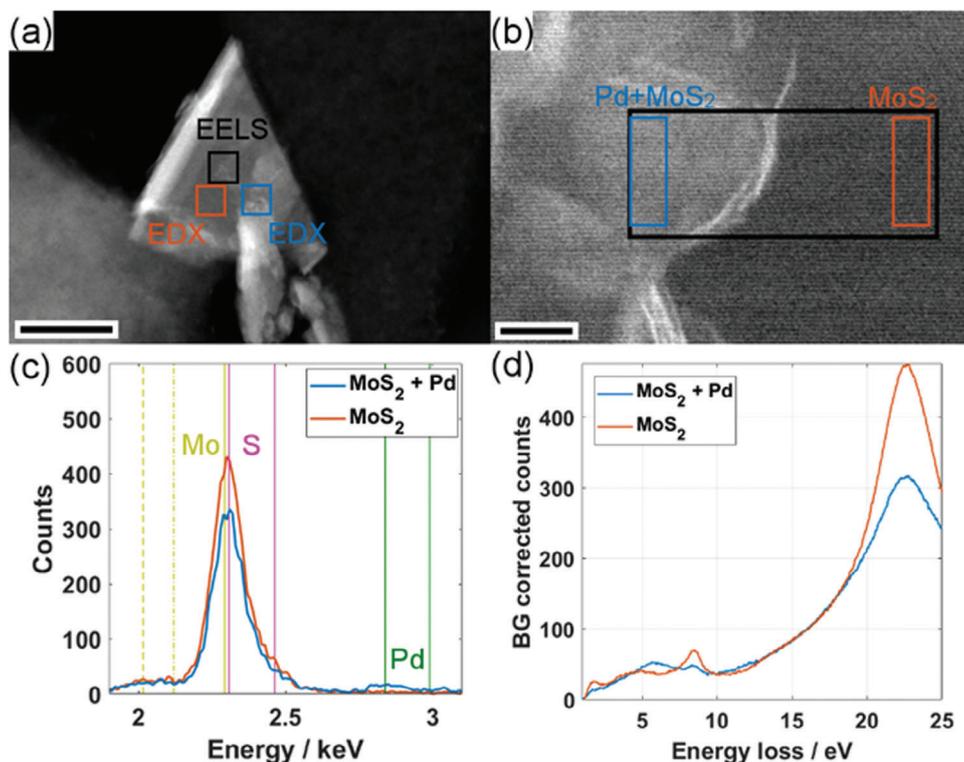
**ADVANCED
SCIENCE NEWS**

www.advancedsciencenews.com

NANO · MICRO

small

www.small-journal.com

Figure 3. Electron spectroscopic analyses of the PdNS@f-MoS$_2$-MalPhBr system. a) DF-STEM image of a flake with attached PdNS and regions for EDX and EELS analyses and b) DF-STEM image of the edge of the PdNS on the flake. c) EDX spectra from the orange (MoS$_2$) and blue (PdNS@f-MoS$_2$-MalPhBr) marked regions in (a) showing the presence of Pd only in the blue region. d) Low-loss EEL spectra from the regions marked in (b) showing the typical signature of MoS$_2$, which is damped in the presence of PdNS. Scale bars are a) 600 nm and b) 20 nm.

the corresponding background-subtracted (power law) EEL spectra are plotted in Figure 3d.

The EEL spectrum obtained from the MoS$_2$ flake without Pd attached corresponds well with literature data on bulk MoS$_2$,[52,53] showing an onset energy of 1.2 eV, a surface plasmon at 8.5 eV, and a bulk plasmon at 22.5 eV. The spectrum obtained in the region of MoS$_2$ and PdNS reveals that the plasmon excitations are damped, the onset energy is not significantly altered and the intensity in the region after the onset energy is redistributed. As the EELS analysis of individual PdNS does not show a response in the energy region below 2 eV (Figure S13, Supporting Information), the observed changes of the MoS$_2$ spectrum when Pd is present can be related to a modification of the properties of MoS$_2$ induced by the functionalization with NIR sensitive PdNS. Additional STEM-EELS analyses confirm this observation and the implied successful functionalization (Figure S14, Supporting Information).

2.3. Exciton Dynamics on Pd-MoS$_2$ Heterostructures

To gain further insights in the photoexcitedstates behaviour within MoS$_2$ nanosheets with and without the covalently linked Pd nanosheets, femtosecond optical transient absorption (TAS) measurements were conducted. **Figure 4a** shows the typical TAS spectrum of MoS$_2$, dominated by a positive $\Delta T/T$ photobleach (PB) signal from A^0 and B^0 excitons at 1.82 and 2 eV, respec-

tively, and the C^0 exciton at the band nesting region around the Λ point (≈ 2.4 eV). The A$^-$ trion is present as a negative $\Delta T/T$ feature (excited state absorption, ESA) at 1.72 eV. Note that due to the strong overlap between A^0 and A$^-$ resonances, the central position of the trion resonance does not correspond with the spectral minimum. PB resonances are already visible within the temporal overlap of pump and probe pulses.[54,55] In the following 1–2 ps, the positive $\Delta T/T$ signal decreases, and ESA resonances emerge. This is followed by a monotonous decrease in intensity and a concurrent blue shift of all spectral features. Beyond 2 ps, the signal decreases without further spectral changes. This spectral evolution agrees with previous reports and has been assigned to hot electron-hole pair cooling followed by diffusion, trapping and band-to-band recombination.[56] The excitonic relaxation was modeled with global fit analysis using a 3-level sequential decay model (details in the Supporting Information and Figure S15, Supporting Information) yielding a sub picosecond lifetime (700 fs) assigned to the hot electron–hole pairs thermalization, a 145 ps lifetime related to diffusion and 1.33 ns lifetime for band-to-band recombination. The obtained electron–hole pair cooling lifetime is in accordance to previous reports in liquid phase exfoliated MoS$_2$,[55,57] but the diffusion related lifetime is approximately a sixfold longer, suggesting that carriers travel 2.5 times larger distances before being trapped.[55]

On the Pd-MoS$_2$, the described MoS$_2$ spectral features are present but shifted tens of meV toward lower energies (A^0 is at 1.8 eV, B^0 is at 1.96 eV). Interestingly, the intensity at the

**ADVANCED
SCIENCE NEWS**

www.advancedsciencenews.com
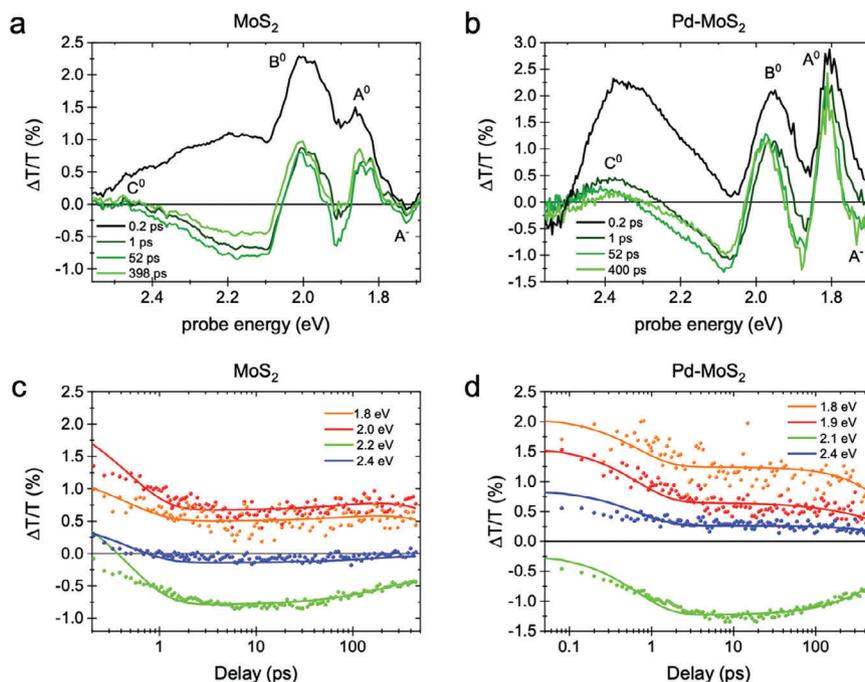
NANO · MICRO
small

www.small-journal.com

Figure 4. $\Delta T/T$ spectra at different delays for a) MoS_2 and b) Pd-MoS_2 heterostructure. Temporal traces at different photon energies of c) MoS_2 and d) Pd-MoS_2 heterostructure of both real data (dots) and global fit analysis (lines).

A^- minimum normalized respecting the A^0 photobleach rises by a 30 %, indicating a higher contribution from trion formation to the TAS spectra when MoS_2 is attached to Pd. Since trion formation depends on the level of doping and higher doping levels shift excitonic resonances toward lower energies,[58] we can interpret these two observations as due to an increase in the MoS_2 doping upon PdNS functionalization.[59] This conclusion is further supported by the analysis of the steady state absorption and the A^- resonance arising on the absorption spectra and the increased relative contribution of a resonance at 1.79 eV to the absorption spectra in the Pd-MoS_2 sample (details in Supporting Information and Figure S16, Supporting Information). Although the measurements indicate an increase of the doping level of the sample, distinguishing between *n*-type and *p*-type remains elusive due to the overlap of the spectral contributions of positive and negative trions.[60] However, transport experiments confirm that the doping observed is *p*-type (see below). A similar global fit analysis on the Pd-MoS_2 was performed, yielding a 500 fs electron–hole pair cooling lifetime, equivalent to the cooling lifetime of bare MoS_2 within our temporal resolution. A diffusion lifetime of 119 ps (18 % faster than in bare MoS_2) suggests the introduction of traps in the MoS_2 upon functionalization. Carrier relaxation was completed with a 939 ps lifetime due to band-to-band recombination.

2.4. On-Device Functionalization

To test the potential extension of the optoelectronic response of PdNS@*f*-MoS_2-MalPhBr toward the infrared region, the functionalization process has been carried out directly on-chip. For the on-device functionalization we employed mechanically exfo-

liated single-layer MoS_2, followed by a similar functionalization process (see the Experimental Section). Additionally, a control experiment was conducted using PdNS@MoS_2 van der Waals structures (depositing the PdNS without any previous organic functionalization, Figure S19, Supporting Information), which was analyzed for comparative purposes. This comparison helps to highlight the differences in performance and characteristics between the two configurations. **Figure 5a** shows Atomic Force Microscopy (AFM) topographic images of the single-layer MoS_2 device after the functionalization process. The inset shows the topography on the same area prior the functionalization. Figure 5b compares two topographic line profiles acquired at the same location on the device (dashed line in Figure 5a) where one can clearly observe an increase on the roughness on the MoS_2 channel upon functionalization, indicating the presence of the PdNS on the MoS_2 surface. An optical image of the final device can be found in the Supporting Information before (Figure S18a, Supporting Information) and after (Figure S18b, Supporting Information) functionalization, which already reveals a change of the flake's surface. AFM characterization confirms roughness changes on the surface, showing a difference in height between 5 and 20 nm, compatible with the presence of the PdNS (Figure 5a,b).

Measurements are performed in a home-built probe station supplemented with a tuneable light source (see the Experimental Section for details) by applying light pulses opening a mechanical shutter for 20 s followed by 20 s with the shutter closed. After each cycle of ON/OFF illumination, the wavelength is increased by 10 nm and the next ON/OFF cycle is carried out. During the measurement, the device is biased with 1 V and the source–drain current is continuously recorded. The photoresponse of the functionalized devices in the NIR, or sometimes referred as short-wave infrared (SWIR), part of the spectrum is relatively modest
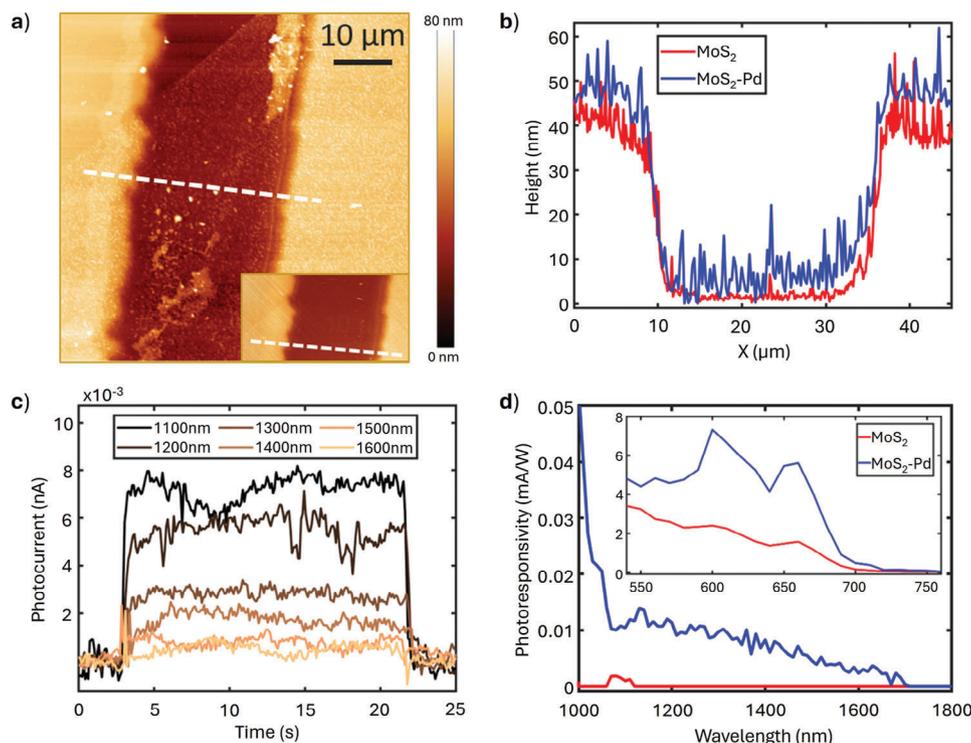
**ADVANCED
SCIENCE NEWS**

www.advancedsciencenews.com

**NANO · MICRO
small**

www.small-journal.com

Figure 5. On-device functionalization and photoresponse. a) AFM topography images of the device consisting of a single layer MoS$_2$ flake transferred onto pre-patterned electrodes after and (inset) before the covalent functionalization with PdNS. b) Topographic line profiles along the white dashed lines drawn in (a), showing the change in roughness after flake functionalization. c) Superimposed photocurrent pulses from 1100 to 1600 nm excitation wavelength with on-times of 20 s and at 1 V bias voltage for the functionalized device. d) Photoresponsivity of a MoS$_2$ device in red and a MoS$_2$ device functionalized in blue in the range 1000–1800 nm (inset 540–760 nm) excitation wavelength and at 1 V bias voltage.

(below 1 mA W^{-1}) and rather fast (see the abrupt jumps when shutter is open/closed in Figure 5c), indicating photoconductivity as the main photogeneration current mechanism.[61–63]

The effect of doping is illustrated in the transfer curves (source–drain current vs gate voltage) in Figure S18c (Supporting Information), where there is an overall shift toward more positive values upon functionalization: the voltage at which the transistor switches to the ON state occurs at higher gate voltages for the functionalized devices. This is caused by hole doping due to the covalent connection through the maleimide linker to the PdNS,[64] which shifts the Fermi level toward the valence band, interestingly in this case allowing to reach the OFF state of the transistor with a threshold voltage around −30 V. The photoresponsivity spectra in the inset of Figure 5d show the excitonic peaks corresponding to a single layer MoS$_2$ around 610 and 660 nm excitation wavelength,[65] similar before and after functionalization meaning transport remains through the MoS$_2$ flake, and with higher photoresponse values due to the increased absorbance for the PdNS@f-MoS$_2$ heterostructure (Figure 1a). For the characterization in the infrared, a 1000 nm log-pass filter is implemented to avoid artefacts due to the second diffraction order (see Figure S18d (Supporting Information), where between 800 and 1000 nm wavelength it is observed the photoresponse due to the second diffraction order in our homebuilt monochromator). Figure 5d shows how the photoresponse of the pristine MoS$_2$ device disappears for excitation wavelengths above 1000 nm, while there is a photoresponse for the functional-

ized device, with decreasing photocurrent upon increasing wavelength as depicted in the light pulses in Figure 5c, until around 1700 nm. This confirms the extension of the absorbance to lower energy spectral regions, making the heterostructure suitable for large range visible/NIR photodetectors.

Interestingly, when a similar MoS$_2$ device was functionalized with PdNS using a van der Waals approach, the behavior was significantly different. In this case, we observed n-doping upon functionalization, instead of p-doping, and the photoresponse is extended to ≈ 1400 nm (Figure S19, Supporting Information,). Moreover, the photoresponse becomes slower upon irradiation. All these features highlight the importance of the covalent linkage in the PdNS@MoS$_2$ heterostructure.

3. Conclusion

In conclusion, we report the synthesis of a chemically connected mixed-dimensional heterostructure composed of PdNS and 2H-MoS$_2$, highlighting its potential application for broadband UV–vis–NIR photodetectors. Key features of the PdNS@f-MoS$_2$ heterostructure include: i) the combination of large lateral size (μm range) and ultrathin thickness (90% of flakes < 5 nm) of MoS$_2$, achieved by a microwave-driven exfoliation method;[42] ii) the morphology of the PdNS (1.5 nm thick and 35 ± 7 nm wide), which is obtained thanks to the capping with CO, resulting in intense SPR absorbance in the NIR region; and iii) the chemical connection between the two nanomaterials, facilitated by a

bifunctional molecule decorated with a maleimide for attachment to MoS_2 and a bromophenyl for connection to PdNS.

The spectroscopic analysis of PdNS@f-MoS_2 reveals electronic interaction between the PdNS and MoS_2, characterized as hole doping based on TAS and electrical measurements. A prototype device fabricated from mechanically exfoliated MoS_2, covalently functionalized in situ, exhibits hole doping and extended photoresponsivity up to 1700 nm, along with a rapid, well-defined response to light pulses after forming the PdNS@f-MoS_2 heterostructure. In contrast, the van der Waals heterojunction demonstrated electron doping, limited photoresponsivity up to 1400 nm and a slower, less defined photoresponse. These findings highlight the effectiveness of this chemical connection strategy in developing nanodimensional heterostructures for photodetection applications.

4. Experimental Section

The exfoliation of bulk 2H-MoS_2 was achieved employing the group's previously established method.[42] In brief, 30 mg of bulk MoS_2 underwent a prewetting phase with 1 mL of ACN, preparing it for further exfoliation. This was followed by its dispersion in 30 mL of NMP and exposure to 300 W microwave irradiation for a duration of 90 s, a process that enabled efficient MoS_2 layer separation due to the rapid and localized heat generated. Notably, this dual-step procedure—ACN prewetting and microwave-driven exfoliation—yielded expansive, ultrathin MoS_2 flakes with significant efficiency. The resultant dispersion was first centrifuged at 2000 rpm for 30 min, with the supernatant decanted to remove unexfoliated residue. The exfoliated MoS_2 was then centrifuged thrice at 10 000 rpm for 30 min each time, with the NMP decanted and replaced with ACN, culminating in a 2D-MoS_2 ACN dispersion.

The exfoliated MoS_2 was functionalized according to a recent protocol developed in the group and here briefly described.[42] A dispersion of exfoliated material (1 mg mL^{-1}) in 10 mL of ACN was set to react with 1 mmol (252 mg) of MalPhBr overnight. Postreaction, the sample was washed with ACN three times to remove any surplus organic molecule.

Ultrathin palladium nanosheets were produced using stainless steel, Teflon lined autoclave. A palladium solution was prepared by mixing 11 mg of Potassium tetrachloropalladate (II) (Sigma-Aldrich), 130 mg of potassium bromide (KBr, Sigma-Aldrich), 12 mg of polyvinyl pyrrolidone (PVP, Merck M_W = 55 000), and 6 mg of cetyltrimethylammonium (CTABr, Merck) in 400 μL of Milli-Q water. Once the previous reagents were solubilized, it was added 3 mL of dimethylformamide (DMF, Merck). The resulting red-colored, homogeneous solution was introduced into the autoclave and gently stirred with a magnetic flea. The autoclave was flushed under CO and pressurized to 6 bars. The autoclave was heated at 80 °C for 40 min. Palladium nanosheets were isolated using acetone as antisolvent and centrifuged for 3 cycles at 5000 rpm for 5 min. The resulting dark blue colloid was redispersed in ACN and preserved in the refrigerator at 5 °C.

The attachment of PdNS to f-MoS_2 was accomplished by gently stirring the two components in ACN for 16 h, facilitated by the bromine-terminated maleimide functionalization. Upon completion of the reaction, purification was carried out through three centrifugation cycles at 10 000 rpm for 10 min each, using ACN to remove unbound PdNS.

TEM images were obtained in Thermo Fisher Scientific Tecnai T20 microscope, operated at 200 kV. HAADF-STEM analyses were conducted at 300 keV electron energy in a Thermo Fisher Scientific Titan Low base with high-brightness gun (X-FEG), monochromator and aberration correction of the electron probe. Acceptance angle for HAADF STEM images was 48 mrad and convergence angle 25 mrad. Energy resolution was 200 meV for monochromated EELS performed with a Gatan imaging filter (GIF, Tridiem ESR 866, Gatan Inc.). Energy-dispersive EDX was obtained with an Oxford Instruments Ultim X-MaxN 100TLE detector. The samples were prepared by drop-casting of a fresh dispersion on TEM holey carbon Cu grids followed by a ligand-cleaning step with activated charcoal and ethanol.

Femtosecond transient absorption spectroscopy measurements were performed using a Ti:Sapphire laser with 120 fs pulse length centered at 775 nm delivering pulses at 1 KHz repetition rate. Pump pulses centered at 387.5 nm were obtained by doubling the frequency of laser output on a BBO crystal and chopped at 500 Hz, blocking one every two pump pulses. Pump fluence was set at 0.1 μJ cm^{-2}, with a 120 fs pulse length and a diameter of 280 μm on the sample. Probe pulses in the 3.2–1.6 eV spectral window were obtained by focusing a fraction of the fundamental on a CaF_2 crystal. Pump and probe beams were spatially overlapped on the sample. The pump–probe delay time was set with a computer-controlled delay line. A spectrometer equipped with a double array optical multichannel detector (Entwicklungsbuero Stresing) operating in single shot acquisition mode was employed to monitor both the transmitted light through the sample and a split-off fraction of the probe as reference. Using a reference channel allows to record the absorption spectrum for each laser shot, thus monitoring the differences in absorbance upon two consecutive pump-on pump-off acquisitions. This approach reduces to half the number of laser pump shots to which the sample is exposed. Measurements were carried out in ambient conditions.

On-device functionalization: the fabrication of the device consisted of a single layer MoS_2 isolated by the mechanical exfoliation of a bulk molybdenite crystal (Molly Hill Mine, Quebec, Canada) with Nitto SPV 224 tape, and consecutive exfoliation onto a Gel-Film stamp (Gel-Film WF 4 × 6.0 mil by Gel-Pack). After the identification of single layer MoS_2 by optical contrast with a metallurgical microscope (Motic BA310 MET-t) and differential reflectance spectroscopy,[66] it is transferred bridging two prepatterned electrodes with a 5 nm Ti adhesion layer and 45 nm Au evaporated onto a (285 nm) SiO_2/Si wafer through a shadow mask from Ossila by dry deterministic transfer.[67] Maleimide functionalization of the MoS_2 flake is then achieved by submerging 16 h the device into a vessel containing 1 mmol of the organic molecule in ACN. Similarly, and after washing the device by dipping it into solutions of water, ethanol, and ACN, the device is immersed into a solution of preformed PdNS in ACN, for another 16 h, as schematically illustrated in Figure S17 (Supporting Information). Washing process is repeated as before.

The electrical characterization is carried out in a home-built probe station setup at ambient conditions. Electrical transport is measured by contacting the contact pads with electrical probes connected to a Keithley 2450 source-measure unit to apply a bias voltage and measure the current. Another probe is brought into contact with the heavily doped silicon and connected to two TENMA power supplies (model 72-2715) to apply positive and negative back gate voltages. The light from a home-built tuneable light source (consisting in a supercontinuum laser coupled to a homemade monochromator) is fiber-coupled into an optical tube lens, which projects a circular-shape light spot with a diameter of around 900 μm onto the device to characterize the photogenerated current.

Supporting Information

Supporting Information is available from the Wiley Online Library or from the author.

Acknowledgements

**ADVANCED
SCIENCE NEWS**

www.advancedsciencenews.com

**NANO · MICRO
small**

www.small-journal.com

Conflict of Interest

The authors declare no conflict of interest.

Author Contributions

V.S., J.S., and E.M.P. supervised the project. R.Q.-O. designed and performed the MoS$_2$ exfoliation, functionalization, and heterostructure experiments. V.S. produced the Pd nanosheets and analyzed the materials by electron microscopy. S.A. performed and analyzed XPS characterization. S.H. performed STEM imaging and spectroscopy analyses supervised by R.A. V.V.-M. and V.B. performed the spectroscopic measurements. V.V.-M. and J.C.-G. analyzed and interpretated the data. P.B., T.P., and A.C.-G. performed on-device experiments and interpretated the data. All authors have discussed the results and drafted on the manuscript.

Data Availability Statement

The data that support the findings of this study are available from the corresponding author upon reasonable request.

[1] A. K. Geim, I. V. Grigorieva, *Nature* **2013**, *499*, 419.

[2] M. Gibertini, M. Koperski, A. F. Morpurgo, K. S. Novoselov, *Nat. Nanotechnol.* **2019**, *14*, 408.

[3] K. S. Novoselov, A. Mishchenko, A. Carvalho, *Science* **2016**, *353*, aac9439.

[4] Y. Liu, N. O. Weiss, X. Duan, H.-C. Cheng, Y. Huang, X. Duan, *Nat. Rev. Mater.* **2016**, *1*, 16042.

[5] P. Wang, C. Jia, Y. Huang, X. J. M. Duan, *Matter* **2021**, *4*, 552.

[6] A. Castellanos-Gomez, X. Duan, Z. Fei, H. R. Gutierrez, Y. Huang, X. Huang, J. Quereda, Q. Qian, E. Sutter, P. Sutter, *Nat. Rev. Method Prim.* **2022**, *2*, 58.

[7] S. Rani, M. Sharma, D. Verma, A. Ghanghass, R. Bhatia, I. Sameera, *Mater. Sci. Semicond. Process* **2022**, *139*, 106313.

[8] A. M. Miller, D. C. Johnson, *J. Mater. Chem. C* **2022**, *10*, 6546.

[9] M.-Y. Li, C.-H. Chen, Y. Shi, L.-J. Li, *Mater. Today* **2016**, *19*, 322.

[10] H. Kumar, D. Er, L. Dong, J. Li, V. B. Shenoy, *Sci. Rep.* **2015**, *5*, 10872.

[11] P. V. Pham, S. C. Bodepudi, K. Shehzad, Y. Liu, Y. Xu, B. Yu, X. Duan, *Chem. Rev.* **2022**, *122*, 6514.

[12] R. Ribeiro-Palau, C. Zhang, K. Watanabe, T. Taniguchi, J. Hone, C. R. Dean, *Science* **2018**, *361*, 690.

[13] G. Bastard, J. Brum, *IEEE J. Quant. Electron.* **1986**, *22*, 1625.

[14] T. Georgiou, R. Jalil, B. D. Belle, L. Britnell, R. V. Gorbachev, S. V. Morozov, Y.-J. Kim, A. Gholinia, S. J. Haigh, O. Makarovsky, L. Eaves, L. A. Ponomarenko, A. K. Geim, K. S. Novoselov, A. Mishchenko, *Nat. Nanotechnol.* **2013**, *8*, 100.

[15] J. Kim, D. Rhee, O. Song, M. Kim, Y. H. Kwon, D. U. Lim, I. S. Kim, V. Mazánek, L. Valdman, Z. Sofer, J. H. Cho, J. Kang, *Adv. Mater.* **2022**, *34*, 2106110.

[16] D. D. Nolte, *J. Appl. Phys.* **1999**, *85*, 6259.

[17] W. Liao, Y. Huang, H. Wang, H. Zhang, *Appl. Mater. Today* **2019**, *16*, 435.

[18] S. Lin, Y. Lu, J. Xu, S. Feng, J. Li, *Nano Energy* **2017**, *40*, 122.

[19] J. Y. Lee, J.-H. Shin, G.-H. Lee, C.-H. Lee, *Nanomaterials* **2016**, *6*, 193.

[20] X. Zhou, X. Hu, J. Yu, S. Liu, Z. Shu, Q. Zhang, H. Li, Y. Ma, H. Xu, T. Zhai, *Adv. Funct. Mater.* **2018**, *28*, 1706587.

[21] N. Huo, Y. Yang, J. Li, *J. Semicond.* **2017**, *38*, 031002.

[22] J. S. Ross, P. Rivera, J. Schaibley, E. Lee-Wong, H. Yu, T. Taniguchi, K. Watanabe, J. Yan, D. Mandrus, D. Cobden, W. Yao, X. Xu, *Nano Lett.* **2017**, *17*, 638.

[23] E. Pomerantseva, Y. Gogotsi, *Nat. Energy* **2017**, *2*, 17089.

[24] Y. Li, J. Zhang, Q. Chen, X. Xia, M. Chen, *Adv. Mater.* **2021**, *33*, 2100855.

[25] P. Das, Q. Fu, X. Bao, Z.-S. Wu, *J. Mater. Chem. A* **2018**, *6*, 21747.

[26] N. Mahmood, I. A. De Castro, K. Pramoda, K. Khoshmanesh, S. K. Bhargava, K. Kalantar-Zadeh, *Energy Storage Mater.* **2019**, *16*, 455.

[27] D. Deng, K. Novoselov, Q. Fu, N. Zheng, Z. Tian, X. Bao, *Nat. Nanotechnol.* **2016**, *11*, 218.

[28] T. A. Shifa, F. Wang, Y. Liu, J. He, *Adv. Mater.* **2019**, *31*, 1804828.

[29] J. Su, G. D. Li, X. H. Li, J. S. Chen, *Adv. Sci.* **2019**, *6*, 1801702.

[30] D. Jariwala, T. J. Marks, M. C. Hersam, *Nat. Mater.* **2017**, *16*, 170.

[31] A. Kagkoura, R. Arenal, N. Tagmatarchis, *Adv. Funct. Mater.* **2021**, *31*, 2105287.

[32] M. Vázquez Sulleiro, A. Develioglu, R. Quirós-Ovies, L. Martín-Pérez, N. Martín Sabanés, M. L. Gonzalez-Juarez, I. J. Gómez, M. Vera-Hidalgo, V. Sebastián, J. Santamaría, E. Burzurí, E. M. Pérez, *Nat. Chem.* **2022**, *14*, 695.

[33] M. Vera-Hidalgo, E. Giovanelli, C. Navio, E. M. Perez, *J. Am. Chem. Soc.* **2019**, *141*, 3767.

[34] H. D. Mai, S. Jeong, T. K. Nguyen, J.-S. Youn, S. Ahn, C.-M. Park, K.-J. Jeon, *ACS Appl. Mater. Interfaces* **2021**, *13*, 14644.

[35] V. Shokhen, D. Zitoun, *Electrochim. Acta* **2017**, *257*, 49.

[36] Z. Cai, B. Liu, X. Zou, H. M. Cheng, *Chem. Rev.* **2018**, *118*, 6091.

[37] S. Tongay, W. Fan, J. Kang, J. Park, U. Koldemir, J. Suh, D. S. Narang, K. Liu, J. Ji, J. Li, R. Sinclair, J. Wu, *Nano Lett.* **2014**, *14*, 3185.

**ADVANCED
SCIENCE NEWS**

www.advancedsciencenews.com

**NANO · MICRO
small**

www.small-journal.com

[38] Yu Zhang, Y. Yao, M. G. Sendeku, L. Yin, X. Zhan, F. Wang, Z. Wang, J. He, *Adv. Mater.* **2019**, *31*, 1901694.

[39] P. S. Toth, M. Velický, T. J. Slater, S. D. Worrall, S. J. J. A. M. T. Haigh, *Appl. Mater. Today* **2017**, *8*, 125.

[40] X.-F. Wang, He Tian, H.-M. Zhao, T.-Y. Zhang, W.-Q. Mao, Y.-C. Qiao, Y. Pang, Y.-X. Li, Y. Yang, T.-L. Ren, *Small* **2018**, *14*, 1702525.

[41] A. Pandey, A. Mukherjee, S. Chakrabarty, D. Chanda, S. Basu, *ACS Appl. Mater. Interfaces* **2019**, *11*, 42094.

[42] R. Quirós-Ovies, M. Laborda, N. M. Sabanés, L. Martín-Pérez, S. M. Da Silva, E. Burzurí, V. Sebastian, E. M. Pérez, J. Santamaría, *ACS Nano* **2023**, *17*, 5984.

[43] V. Sebastian, C. D. Smith, K. F. Jensen, *Nanoscale* **2016**, *8*, 7534.

[44] R. Quirós-Ovies, M. Vázquez Sulleiro, M. Vera-Hidalgo, J. Prieto, I. J Gómez, V. Sebastián, J. Santamaría, E. M. Pérez, *Chem. – Eur. J.* **2020**, *26*, 6629.

[45] N. Miyaura, A. Suzuki, *Chem. Rev.* **1995**, *95*, 2457.

[46] Y.-S. Li, S. Li, *Spectrochim. Acta A* **1994**, *50*, 509.

[47] M. Ziolek, O. Saur, J. Lamotte, J.-C. Lavalley, *J. Chem. Soc., Faraday Trans.* **1994**, *90*, 1029.

[48] L. Uson, C. Yus, G. Mendoza, E. Leroy, S. Irusta, T. Alejo, D. García-Domingo, A. Larrea, M. Arruebo, R. Arenal, V. Sebastian, *Adv. Funct. Mater.* **2022**, *32*, 2270058.

[49] J. F. Moulder, J. Chastain, *Handbook of X-ray Photoelectron Spectroscopy: A Reference Book of Standard Spectra for Identification and Interpretation of XPS Data: Physical Electronics Division*, Perkin-Elmer Corporation, Shelton, CT **1992**.

[50] D. Schild, *Hydrogen Technology: Mobile and Portable Applications* (Ed: A. Léon), Springer, Heidelberg, **2008**, pp. 575–601.

[51] I. Rosa-Pardo, D. Zhu, A. Cortés-Villena, M. Prato, L. De Trizio, L. Manna, R. E. Galian, J. Pérez-Prieto, *ACS Energy Lett.* **2023**, *8*, 2789.

[52] H. C. Nerl, K. T. Winther, F. S. Hage, K. S. Thygesen, L. Houben, C. Backes, J. N. Coleman, Q. M. Ramasse, V. Nicolosi, *npj 2D Mater. Appl.* **2017**, *1*, 2.

[53] M. Pelaez-Fernandez, Y.-C. Lin, K. Suenaga, R. Arenal, *Nanomaterials* **2021**, *11*, 3218.

[54] A. Kormányos, G. Burkard, M. Gmitra, J. Fabian, V. Zólyomi, N. D. Drummond, V. Fal'ko, *2D Mater.* **2015**, *2*, 049501.

[55] V. Vega-Mayoral, T. Borzda, D. Vella, M. Prijatelj, E. A. A. Pogna, C. Backes, J. N. Coleman, G. Cerullo, D. Mihailovic, C. Gadermaier, *2D Mater.* **2018**, *5*, 015011.

[56] T. Borzda, C. Gadermaier, N. Vujicic, P. Topolovsek, M. Borovsak, T. Mertelj, D. Viola, C. Manzoni, E. A. A. Pogna, D. Brida, M. R. Antognazza, F. Scotognella, G. Lanzani, G. Cerullo, D. Mihailovic, *Adv. Funct. Mater.* **2015**, *25*, 3351.

[57] V. Vega-Mayoral, D. Vella, T. Borzda, M. Prijatelj, I. Tempra, E. A. A. Pogna, S. Dal Conte, P. Topolovsek, N. Vujicic, G. Cerullo, D. Mihailovic, C. Gadermaier, *Nanoscale* **2016**, *8*, 5428.

[58] K. F. Mak, K. He, C. Lee, G. H. Lee, J. Hone, T. F. Heinz, J. Shan, *Nat. Mater.* **2013**, *12*, 207.

[59] A. Chernikov, A. M. van der Zande, H. M. Hill, A. F. Rigosi, A. Velauthapillai, J. Hone, T. F. Heinz, *Phys. Rev. Lett.* **2015**, *115*, 126802.

[60] M. Drüppel, T. Deilmann, P. Krüger, M. Rohlfing, *Nat. Commun.* **2017**, *8*, 2117.

[61] M. M. Furchi, D. K. Polyushkin, A. Pospischil, T. Mueller, *Nano Lett.* **2014**, *14*, 6165.

[62] J. O. Island, S. I. Blanter, M. Buscema, H. S. J. van der Zant, A. Castellanos-Gomez, *Nano Lett.* **2015**, *15*, 7853.

[63] D. Kufer, G. Konstantatos, *Nano Lett.* **2015**, *15*, 7307.

[64] J. Miao, L. Wu, Z. Bian, Q. Zhu, T. Zhang, X. Pan, J. Hu, W. Xu, Y. Wang, Y. Xu, B. Yu, W. Ji, X. Zhang, J. Qiao, P. Samorì, Y. Zhao, *ACS Nano* **2022**, *16*, 20647.

[65] J. Zhang, L. Yao, N. Zhou, H. Dai, H. Cheng, M. Wang, L. Zhang, X. Chen, X. Wang, T. Zhai, J. Han, *J. Phys. Chem. C* **2019**, *123*, 11216.

[66] Y. Niu, S. Gonzalez-Abad, R. Frisenda, P. Marauhn, M. Drüppel, P. Gant, R. Schmidt, N. S. Taghavi, D. Barcons, A. J. Molina-Mendoza, S. M. de Vasconcellos, R. Bratschitsch, D. P. De Lara, M. Rohlfing, A. Castellanos-Gomez, *Nanomaterials* **2018**, *8*, 725.

[67] A. J. Molina-Mendoza, E. Giovanelli, W. S. Paz, M. A. Niño, J. O. Island, C. Evangeli, L. Aballe, M. Foerster, H. S. J. van der Zant, G. Rubio-Bollinger, N. Agraït, J. J. Palacios, E. M. Pérez, A. Castellanos-Gomez, *Nat Commun.* **2017**, *8*, 14409.